

Spin-orbit coupling and spin relaxation of hole states in [001]- and [111]-oriented quantum dots of various geometry

Krzysztof Gawarecki* and Mateusz Krzykowski

*Department of Theoretical Physics, Faculty of Fundamental Problems of Technology,
Wrocław University of Technology, Wybrzeże Wyspiańskiego 27, 50-370 Wrocław, Poland*

We study the influence of spin-orbit coupling on the hole states in InAs/GaAs quantum dots grown on [001]- and [111]-oriented substrates belonging to symmetry point groups: C_{2v} , C_{3v} and D_{2d} . We investigate the impact of various spin-orbit mechanisms on the strength of coupling between s - and p -shell states, which is a significant spin-flip channel in quantum dots. We calculate spin relaxation rates between the states of lowest Zeeman doublet and show that the [111]-oriented structure offers one order of magnitude slower relaxation compared to the usual [001]-oriented self-assembled QD. The magnetic-field dependence of the hole states is calculated using multiband (up to 14 bands) $\mathbf{k}\cdot\mathbf{p}$ model. We identify the irreducible representations linked to the states and discuss the selection rules, which govern the avoided-crossing pattern in magnetic-field dependence of the energy levels. We show that dominant contribution to the coupling between some of these states comes from the shear strain. On the other hand, we demonstrate no coupling between s - and p -shell states in the [111]-oriented structure.

I. INTRODUCTION

The properties of nanostructures related to the spin degree of freedom are interesting from the point of view of possible applications in quantum information processing and spintronics¹⁻⁴. Coupling of spin to orbital degrees of freedom via the spin-orbit coupling (SOC) influences the carrier spectrum and could provide a channel of quantum coherent spin control⁵. On the other hand, it may mix spin configurations, which leads to spin relaxation and dephasing processes⁶⁻¹¹. The lack of inversion symmetry, on the level of crystal lattice (bulk inversion asymmetry, BIA), in the shape of a nanostructure, or induced by external electric field (structure inversion asymmetry, SIA) gives rise to Dresselhaus and Rashba spin-orbit coupling, respectively¹². Furthermore, recent investigations show hidden spin polarization in centrosymmetric crystals¹³.

Dresselhaus and/or Rashba interactions are commonly accounted for theoretically within effective models¹⁴⁻¹⁷. While the parameters are available and well established for bulk materials, in the case of nanostructures the coupling strength is determined by their shape, composition profile, substrate orientation, strain and abrupt material interfaces. In consequence, a reliable quantitative description of the SIA effects requires advanced modeling. The impact of Dresselhaus and Rashba couplings on carrier states in a quantum dot (QD) were studied in various approaches¹⁴⁻¹⁸. In the case of InAs/GaAs self-assembled QDs, the influence of spin-orbit coupling is more complicated due to the presence of interfaces abrupt and symmetry-breaking shear strain. The latter gives spin admixture leading to electron spin relaxation¹⁹ and this is one of the most important factors determining the splitting between hole p -type states¹⁸. Symmetry of the self-assembled QD plays crucial role for its optical properties and exchange interaction^{20,21}. It has been also shown that the coupling between s - and p -shell electron states related to the Rashba interaction is enhanced by

the dot anisotropy^{15,16}. Furthermore, the symmetry determines anticrossing pattern²²⁻²⁴ as well as affects spin mixing and relaxation in a double QD system^{11,25}. The properties of the nanostructure depends not only on its geometrical shape but also orientation of the underlying substrate. Due to potential application for entangled photon pairs generation, [111]-oriented QDs were subject of many theoretical and experimental works²⁶⁻³³.

The phonon-induced spin-flip of carriers in QDs was investigated in many theoretical^{10,14,34-36} and experimental works³⁷⁻³⁹. This effect results from the direct spin-phonon coupling⁴⁰ and from spin-admixture mechanisms^{6,7}. The latter is related to the fact, that in presence of the spin-orbit interaction, the state with a given nominal spin orientation, contains a non-zero component of opposite spin. Due to this admixture, even diagonal part of the carrier-phonon Hamiltonian gives rise to the spin-flip effect. In fact, it has been shown for the electron and hole in 2D GaAs QD, that near the avoided crossing between s and p states (where p -type spin admixture to the s -type state becomes large) the spin-flip transition rate dramatically increases^{14,35}. Also, the orientation of magnetic field with respect to crystallographic axes strongly affects spin relaxation time in gate-defined GaAs QDs, which was attributed to the interplay of Rashba and Dresselhaus couplings³⁹. This was addressed theoretically for [001]- and [111]-grown GaAs cuboidal QDs⁴¹. Furthermore, in Ref. 34 hole spin relaxation is studied for a QD defined by a parabolic potential in GaAs quantum well (QW) of various crystal orientation. The influence of strain on spin-flip transitions was investigated. It has been shown, that for [001]-grown structure, the biaxial strain affects spin relaxation indirectly, by changing the energy difference between heavy- and light-hole subbands. On the other hand, for QD in [111]-oriented QW, strain provides a direct spin mixing channel. Furthermore, such a structure, offers longer spin relaxation time (compared to the [001]-oriented one) at the regime of strong confinement in growth direction³⁴.

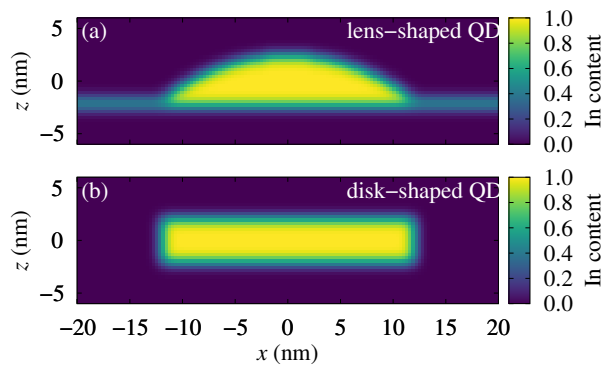


FIG. 1. (Color online) Material distribution in the system, in the case of lens- (a) and disk-shaped (b) QD.

In this work, we investigate the influence of various mechanisms (Dresselhaus and Rashba interaction, shear strain) on the coupling between the s - and p -shell hole states in InAs/GaAs QDs. Within the 8-band $\mathbf{k}\cdot\mathbf{p}$ model, we calculate the magnetic-field dependence of the energy levels and study the width of avoided crossing between the s - and p -type state. We take into account [001]- and [111]-oriented substrates and consider three types of QDs representing C_{2v} , C_{3v} and D_{2d} symmetry point groups. For these, we identify the irreducible representations of hole states, discuss the selection rules, and demonstrate the absence of coupling between s and both p -shell states for the [111]-oriented structure. Finally, we show that spin-flip transitions at low magnetic fields are slower by an one order of magnitude for [111]-oriented QD compared to the standard [001]-oriented system.

The paper is organized as follows. In Sec. II, the methods used to calculate the strain distribution and the carrier states are described. In Sec. III, we present the results of numerical simulations for all of the considered structures. The phonon-induced spin relaxation is discussed in Sec. IV. Finally, Sec. V contains the summary. In Appendix A we present character tables of the symmetry point groups used in the paper. In Appendix B, we describe the effective model with empirical parameters which are fitted to the numerical data.

II. MODEL

The system under consideration contains a single InAs/GaAs QD. We model lens- and disk-shaped QDs [see Fig. 1(a,b)]. In both cases, the dot height is $h = 4.2$ nm and the base radius is $r = 12$ nm. Furthermore, the lens-shaped dot is placed on a 0.6 nm thick wetting layer.

The distribution of strain in the system is calculated within the continuous elasticity approach⁴². To calculate the strain tensor elements for the [111]-grown system, we perform transformation to the rotated coordinates³¹.

The piezoelectric potential is calculated up to the second order in the strain tensor elements⁴³ with parameters taken from Ref. 44, while transformation to the [111]-oriented system is performed following Ref. 31.

The hole states are calculated using 8- and 14-band $\mathbf{k}\cdot\mathbf{p}$ method in the envelope function approximation (if not stated otherwise, we take into account 8 bands). The full 14-band Hamiltonian can be divided into the blocks corresponding to the irreducible representations of T_d symmetry point group: Γ_{8c} , Γ_{7c} , Γ_{6c} , Γ_{8v} , or Γ_{7v} ^{12,18,45}

$$H = \begin{pmatrix} H_{8c8c} & H_{8c7c} & H_{8c6c} & H_{8c8v} & H_{8c7v} \\ H_{7c8c} & H_{7c7c} & H_{7c6c} & H_{7c8v} & H_{7c7v} \\ H_{6c8c} & H_{6c7c} & H_{6c6c} & H_{6c8v} & H_{6c7v} \\ H_{8v8c} & H_{8v7c} & H_{8v6c} & H_{8v8v} & H_{8v7v} \\ H_{7v8c} & H_{7v7c} & H_{7v6c} & H_{7v8v} & H_{7v7v} \end{pmatrix},$$

where highlighted part corresponds to the standard 8-band $\mathbf{k}\cdot\mathbf{p}$ Hamiltonian. The states are then 8- or 14-component pseudo-spinors, where each part refers to one of the subbands. The full Hamiltonian, parameters and details of numerical implementation are presented in the Appendix of Ref. 18. We account for an axial electric field by adding a diagonal term $H^{(\text{Efield})} = |e|Fz$ to the Hamiltonian, where e is the elementary charge and F is the field magnitude. To model [111]-oriented system, we rotate the Hamiltonian transforming all vectors and invariant matrices (see a detailed description in Ref. 45). The average values of the z projection of the hole envelope angular momenta are calculated from

$$\langle M_z \rangle = \sum_{m=1}^8 \int_{-\infty}^{\infty} \psi_{n,m}^*(\mathbf{r}) \left(iy \frac{\partial}{\partial x} - ix \frac{\partial}{\partial y} \right) \psi_{n,m}(\mathbf{r}) d\mathbf{r}.$$

where $\psi_{n,m}(\mathbf{r})$ denotes the m -th band component of the n -th hole wave function.

The 14-band $\mathbf{k}\cdot\mathbf{p}$ model accounts inherently for the Dresselhaus and Rashba couplings¹². Also the 8-band model contains the most important terms for the Rashba coupling, while the Dresselhaus interaction is described by perturbative elements explicitly added to H_{6c8v} and H_{6c7v} . The Dresselhaus SOC Hamiltonian for the electron (in 2-band $\mathbf{k}\cdot\mathbf{p}$ model) can be approximated by $H_{6c6c}^{(D)} \propto \langle k_z^2 \rangle (k_+ \sigma_+ + k_- \sigma_-)$, where $k_{\pm} = k_x \pm ik_y$, and σ_{\pm} is the spin ladder operator. This couples $|M_z \approx 0, \downarrow\rangle$ to $|M_z \approx 1, \uparrow\rangle$ and $|M_z \approx 0, \uparrow\rangle$ to $|M_z \approx -1, \downarrow\rangle$, where \uparrow, \downarrow refers to the spin orientation. In contrast, the Rashba coupling approximated by $H_{6c6c}^{(R)} \propto i(k_+ \sigma_- - k_- \sigma_+)$ connects $|M_z \approx 0, \uparrow\rangle$ to $|M_z \approx 1, \downarrow\rangle$, and $|M_z \approx 0, \downarrow\rangle$ to $|M_z \approx -1, \uparrow\rangle$. On the other hand, the influence of the spin-orbit interaction for holes is much more complicated compared to the electron¹². In this case, the Rashba coupling may mix $|M_z \approx 0, \uparrow\rangle$ to both $|M_z \approx 1, \downarrow\rangle$ and $|M_z \approx -1, \downarrow\rangle$ (and vice-versa), where \uparrow, \downarrow refers to band angular momentum (see Appendix B).

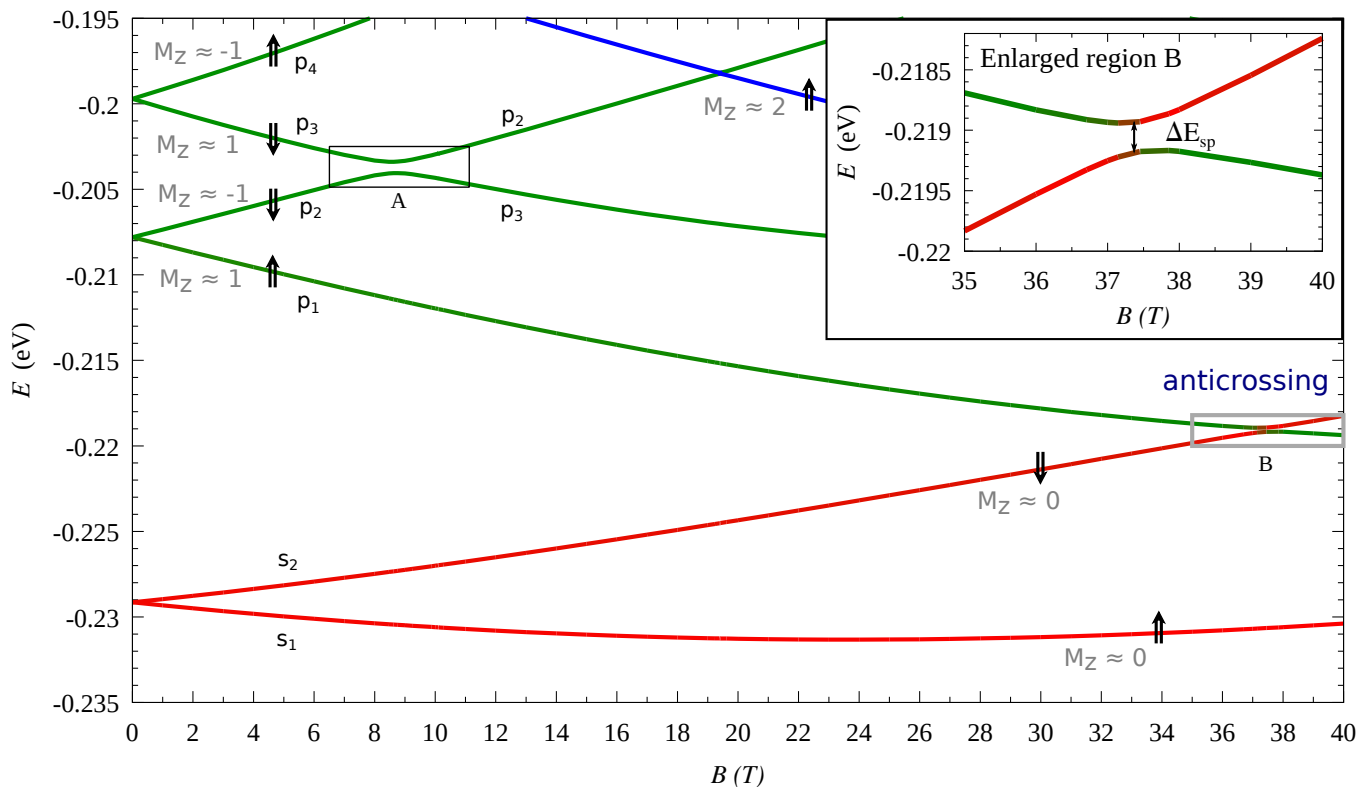


FIG. 2. (Color online) Magnetic-field dependence of the lowest hole energy levels for the lens shaped [001]-oriented QD. The inset contains enlarged part of the plot with anticrossing between s - and p -type states. Energy $E = 0$ refers to the unstrained GaAs valence-band edge.

III. NUMERICAL RESULTS AND SYMMETRY CLASSIFICATION

A. [001]-oriented lens shaped QD

We calculated the magnetic-field dependence of the lowest-energy hole states in the lens-shaped QD. The shape of such a structure does not have the inversion symmetry. The energy levels obtained from 8-band $\mathbf{k}\cdot\mathbf{p}$ simulations are presented in Fig. 2. Although the states contain contributions of various envelope symmetry (which results from the subband mixing), they can be labeled as s , p , d , ... with respect to the dominant component (read from the value of $\langle M_z \rangle$). The two lowest-energy states (marked by the red lines) exhibit s -type symmetry, their average value of the axial projection of envelope angular momentum $\langle M_z \rangle$ is close to 0. The next four states (plotted with green lines) exhibit p -type symmetry with $\langle M_z \rangle \approx \pm 1$. Although the shape of the QD transforms according to the $C_{\infty v}$ group, the underlying crystal lattice limits the symmetry of the system to the C_{2v} (at $B = 0$ T). Due to the spin-orbit coupling, the system must be described in terms of the double group representations^{46–48}. The symmetry point group C_{2v} contains only one irreducible double group representation $D_{1/2}$ (see the character table in Appendix A) and all

states must belong to it. Since $D_{1/2}$ is two-dimensional, the states are doubly degenerate (which in fact results from the time-reversal symmetry). At nonzero axial magnetic field $B \neq 0$, the symmetry of the system is further reduced to C_2 ^{11,12}. In this case, $D_{1/2}$ splits into two one-dimensional representations: D_A and D_B , where $D_A = D_B^*$ (see Tab. III in Appendix A). For each state $|\Psi\rangle$ we found the relevant irreducible representation α via projection $\hat{P}^{(\alpha)}|\Psi\rangle$, where $\hat{P}^{(\alpha)} = \sum_i \chi^*(\hat{R}_i)\hat{R}_i$, and $\chi(\hat{R}_i)$ is the character of the representation α for the symmetry operation \hat{R}_i ^{46,49}. The states s_1 , p_2 and p_3 belong to D_A , whereas s_2 , p_1 and p_4 to D_B . According to the selection rules, two states can couple if they belong to the same irreducible representation. In the presence of SOC, an avoided crossing pattern appears in the system spectrum. In the considered system, the spin-orbit coupling in the hole p shell favors the parallel orientation of the envelope and band angular momenta (see a detailed discussion in Ref. 18). At $B \approx 9$ T, there is an avoided crossing between p_2 and p_3 (region A in Fig. 2), they have the same orientation of the band angular momenta but different M_z . Furthermore, an avoided crossing appears between states s_2 ($\langle M_z \rangle \approx 0, \downarrow$) and p_1 ($\langle M_z \rangle \approx 1, \uparrow$) at region B, where its width is $\Delta E_{sp} = 0.246$ meV.

To assess the importance of various SOC mechanisms and check the accuracy of 8-band $\mathbf{k}\cdot\mathbf{p}$, we compared the

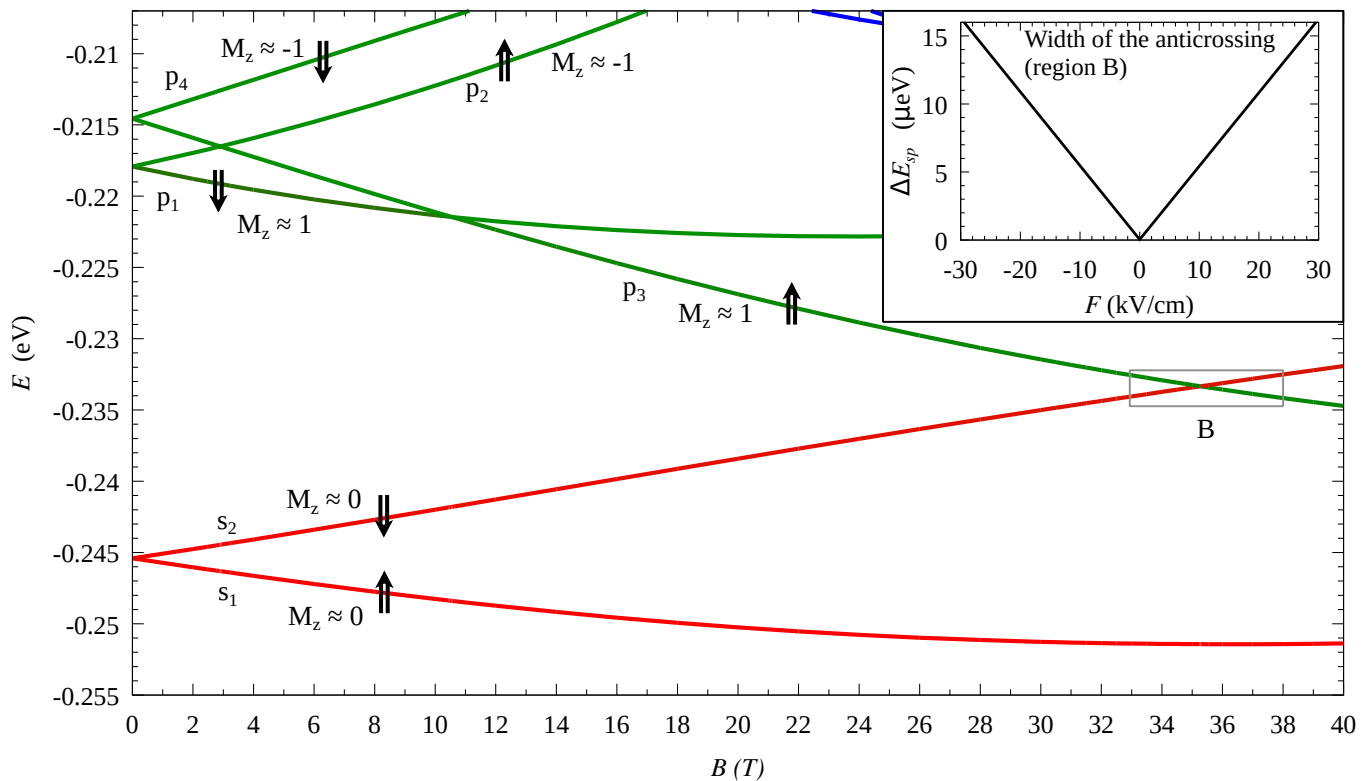


FIG. 3. (Color online) Magnetic-field dependence of the lowest hole energy levels for the disk shaped [001]-oriented QD. The inset contains the avoided crossing width between s - and p -shell energy levels as a function of external axial electric field F .

value of ΔE_{sp} obtained within several degrees of approximation. As shown in Tab. I, the results from 8- and 14-band $\mathbf{k}\cdot\mathbf{p}$ are in a good agreement. Dresselhaus terms are negligible for ΔE_{sp} , however they could be important for $s_1 - p_3$ and $s_2 - p_4$ couplings (which is hard to estimate, because it is not represented by any avoided crossing in the considered spectrum). In the last approach, the influence of shear strain in the valence band is neglected by setting the deformation potential $d_v = 0$. In this case, ΔE_{sp} is significantly reduced, which suggest that the shear strain is one of the most important factors determining the $s - p$ coupling.

TABLE I. The anticrossing width ΔE_{sp} between s and p -type state obtained from various approximations.

Model	ΔE_{sp} (meV)
14-band $\mathbf{k}\cdot\mathbf{p}$, full	0.25481
8-band $\mathbf{k}\cdot\mathbf{p}$, full	0.24627
8-band $\mathbf{k}\cdot\mathbf{p}$, Dresselhaus terms $H^{(D)} = 0$ neglected	0.24565
8-band $\mathbf{k}\cdot\mathbf{p}$, shear strain neglected ($d_v = 0$)	0.11679

The Rashba coupling can rise due to external potentials. We calculated ΔE_{sp} at the axial electric field $F = 30$ kV/cm and obtained $\Delta E_{sp} = 0.243$ meV, while opposite direction $F = -30$ kV/cm led to $\Delta E_{sp} = 0.248$ meV. This shows, that for the considered QD the axial elec-

tric field generates the Rashba coupling, which is much weaker than the structure inversion asymmetry resulting from the QD shape.

B. [001]-oriented disk shaped QD

The magnetic-field dependence of energy levels calculated for the [001]-oriented disk-shaped QD is presented in Fig. 3. For such a system, at $B = 0$, the symmetry point group is D_{2d} . According to the character table (Tab. IV in Appendix A), there are two irreducible double-group representations $D_{1/2}$ and D' . In the presence of magnetic field, the symmetry of the system is reduced to S_4 (see Tab. V in Appendix A)¹². Then, the states s_1 and p_1 belong to D_I , s_2 and p_2 to D_{II} , p_3 to D_{IV} , and p_4 to D_{III} representation. Since s_2 and p_3 states belong to different representations, there is no avoided crossing between their energy levels (see region B in Fig. 3). For the same reason, we obtain a crossing between p_2 and p_3 at about 3 T. In contrast to the lens-shaped QD, at weak magnetic field, the states with antiparallel envelope and band angular momenta have lower energy compared to the opposite configuration.

The symmetry of the system can be further reduced by external electric field. For axial field, the symmetry changes from D_{2d} to C_{2v} (and from S_4 to C_2 at $B \neq 0$). In this case, the Rashba coupling between upper s -shell

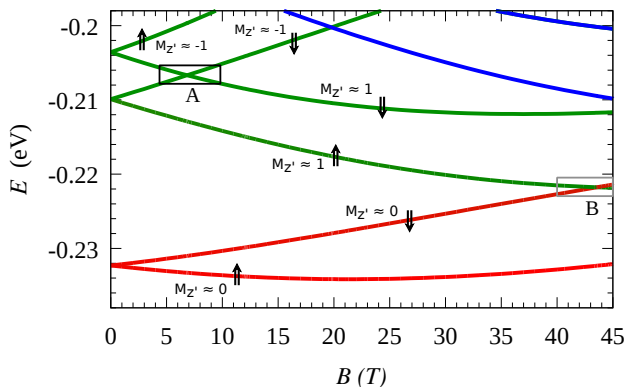


FIG. 4. (Color online) Magnetic field dependence of the lowest hole energy levels for the lens shaped [111]-oriented QD.

state ($M_z \approx 0, \downarrow$) and the p -shell state ($M_z \approx 1, \uparrow$) appears. The simulation results are presented in the inset of Fig. 3. The width of the anticrossing increases linearly with the electric field, and at $F = 0$ there is a crossing between the relevant energy levels.

C. [111]-oriented lens shaped QD

Finally, we investigate the magnetic-field dependence for a lens-shaped QD grown in the [111] direction. The simulation results are presented in Fig. 4. At $B = 0$, the symmetry of the system is C_{3v} , while the axial magnetic field (now oriented along the [111] direction) reduces it to C_3 (see character tables in Appendix A). This leads to different selection rules compared to the cases considered previously. We identified the representations of the states: s_1 and s_2 belong to D_I , p_1 and p_3 to D_{II} , while p_2 and p_4 to D_{III} . In consequence, there is no avoided crossing between p_2 and p_3 energy branches (see region A in Fig. 4). Furthermore, s - and p -type states are decoupled and there is a crossing between their energy levels (a very small anticrossings in the simulation results are numerical artifacts related to the discretization on a rectangular mesh). In contrast to the [001]-oriented disk-shaped QD, the crossing between s_2 and p_1 energy branches can not be resolved by the axial electric field because it does not change the symmetry of the system.

IV. PHONON-ASSISTED SPIN RELAXATION

We account for the hole-phonon coupling within the long-wavelength limit. The phonon-induced spin-flip rate between the states $|\psi_i\rangle$ and $|\psi_j\rangle$ at zero temperature is calculated using the Fermi golden rule

$$\gamma_{ij} = \frac{2\pi}{\hbar^2} \sum_{\lambda, \mathbf{q}} |\langle \psi_j | \mathcal{V}_{\text{int}}(\mathbf{q}, \lambda) | \psi_i \rangle|^2 \delta \left(\frac{\Delta E_{ij}}{\hbar} - c_\lambda q \right),$$

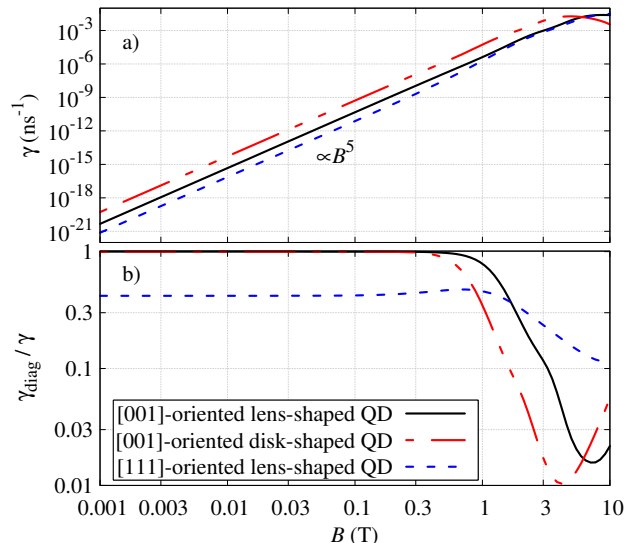


FIG. 5. (Color online) (a) Phonon-assisted spin relaxation rate in the lowest-energy Zeeman doublet as a function of magnetic field for [001]- and [111]-oriented QDs; (b) ratio of the relaxation rate from spin-admixture mechanisms to the overall relaxation rate.

where \mathbf{q} is a wave vector, λ denotes an acoustic phonon branch, ΔE_{ij} is the energy difference between the states, and c_λ is a polarization-dependent speed of sound in GaAs. Finally, $\mathcal{V}_{\text{int}}(\mathbf{q}, \lambda) = \mathcal{H}_{\text{B-P}}^{(\text{ph})}(\mathbf{q}, \lambda) + \mathcal{H}_{\text{PZ}}^{(\text{ph})}(\mathbf{q}, \lambda)$ is a Hamiltonian of hole-phonon interaction containing the couplings via deformation potential (represented by the 8-band Bir-Pikus Hamiltonian $\mathcal{H}_{\text{BP}}^{(\text{ph})}$) and via the phonon-induced piezoelectric potential $\mathcal{H}_{\text{PZ}}^{(\text{ph})}$, both written in terms of phonon modes (\mathbf{q}, λ) . The details are given in Refs. 9, 36, and 50. The rotation to [111]-oriented coordinate system is performed in a standard way, by transforming strain tensor and invariant matrices.

We calculated phonon-assisted spin relaxation rate from s_2 to s_1 state ($\gamma \equiv \gamma_{21}$) for all of the considered QD structures [Fig. 5(a)]. For weak magnetic field, the relaxation rate in the [111]-oriented lens-shaped QD is one order of magnitude lower compared to the dot with the same geometry but the [001] substrate orientation. This results from the suppression of the p -type admixtures ($M_z = \pm 1$) in the heavy-hole components of wave functions in the [111]-oriented QD. Furthermore, up to $B \approx 6$ T relaxation in the disk-shaped QD is faster compared to the lens-shaped. This can be related to greater g -factor (hence larger transition energy at given value of B) in the disk-shaped QD. Finally, at high magnetic field, all of the rates saturate and then decrease, which is caused by the phonon spectral density suppression at high frequency regime. Since for all of the considered structures the s - p anticrossing appears at high magnetic field, we do not observe relaxation peaks characteristic

for the 2D GaAs QD^{14,35}. Increase of the spin relaxation time for the [111] crystal orientation has been demonstrated (in the regime of strong confinement in growth direction) in a QD defined by harmonic potential in a QW³⁴. In contrast to the QDs in quantum well considered in that paper, the strain field in self-assembled QDs contains nonzero shear components for any crystal orientation. Shear strain enters the hole Hamiltonian with the d_v deformation potential. In consequence, even for the [001]-oriented structure, we have a direct strain-related channel of spin admixture, which is important for the spin relaxation process.

We calculated the ratio $\gamma_{\text{diag}}/\gamma$, where γ_{diag} is the transition rate due to all spin-admixture mechanisms, obtained by taking only the spin-diagonal part of \mathcal{V}_{int} . As shown in Fig.5(b), for the [001]-oriented structures the spin-admixture mechanisms dominates at low and moderate magnetic-fields. In contrast, for such fields in [111]-oriented structure the spin-admixture part is strongly reduced and direct spin-phonon coupling is relevant in the whole B range. To quantitatively assess the importance of various symmetry contributions to the coupling via spin admixture, we perform an analysis based on spherical harmonics. The spin-admixture (diagonal) part of the Hamiltonian at low magnetic fields is dominated by the piezoelectric potential coupling⁹. The relevant part of the Hamiltonian can be written as

$$\langle \psi_j | \mathcal{H}_{\text{PZ}}^{(\text{ph})}(\mathbf{q}, \lambda) | \psi_i \rangle = M_\lambda(\hat{\mathbf{q}}) \mathcal{F}_{ij}(\mathbf{q}),$$

where $M_\lambda(\hat{\mathbf{q}})$ is a polarization-dependent geometric factor⁵¹, and \mathcal{F}_{ij} is a form-factor defined by

$$\mathcal{F}_{ij}(\mathbf{q}) = \sum_{s=1}^8 \int_{-\infty}^{\infty} \psi_{i,s}^*(\mathbf{r}) \psi_{j,s}(\mathbf{r}) e^{i\mathbf{q}\mathbf{r}} d\mathbf{r}.$$

The form-factor $\mathcal{F} \equiv \mathcal{F}_{12}$ can be written in spherical coordinates $\mathcal{F}(q, \theta, \phi)$. To obtain values at desired points, we use nonuniform fast Fourier transform in our numerical calculations (NUFFT library)⁵². Then, the form-factor is expanded in spherical harmonics

$$\mathcal{F}(q, \theta, \phi) = \sum_{m,l} a_{lm}(q) Y_l^m(\theta, \phi),$$

where

$$a_{lm}(q) = \int_0^{2\pi} d\phi \int_0^\pi \sin \theta Y_l^{m*}(\theta, \phi) \mathcal{F}(q, \theta, \phi) d\theta.$$

We calculated $a_{lm}(q)$ coefficients and $W_{lm} = |a_{lm}|^2/\mathcal{N}$, where

$$\mathcal{N} = \int_0^{2\pi} d\phi \int_0^\pi \sin \theta |\mathcal{F}(q, \theta, \phi)|^2 d\theta.$$

Since $\mathcal{F}(\mathbf{q})$ contains the product of states, the resulting symmetry depends on the relative importance of subbands and their envelopes. Figs.6(a-c) present the results

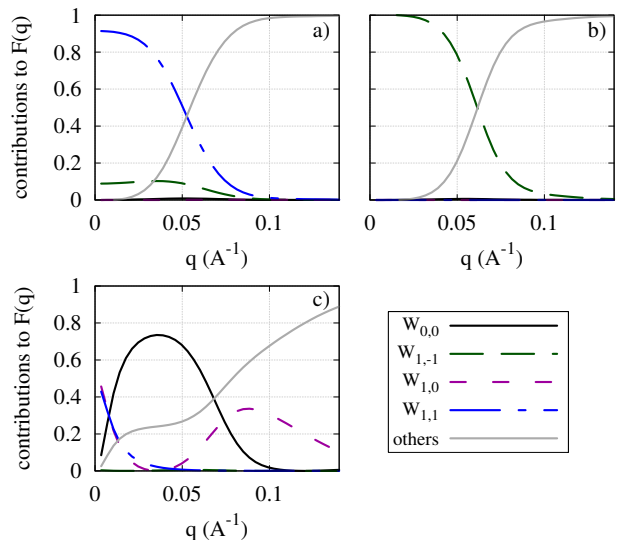


FIG. 6. (Color online) Form-factor $F(q)$ expansion in spherical harmonics for (a) [001]-oriented lens- and (b) disk-shaped QD, and (c) [111]-oriented lens-shaped QD.

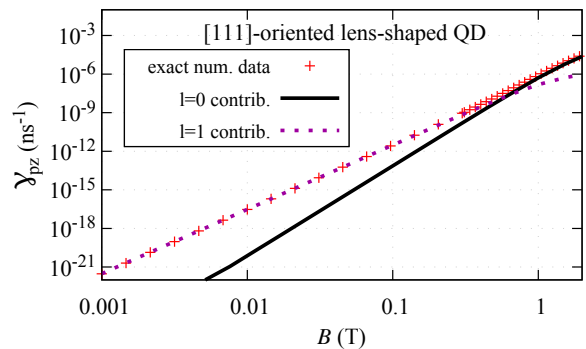


FIG. 7. (Color online) Phonon-assisted spin relaxation rate due to coupling via piezoelectric potential; red points denotes results obtained taking numerically exact $F(q)$, for the black solid line $F(q) \approx a_{0,0} Y_0^0$, and for the blue dashed line $F(q) \approx a_{1,-1} Y_1^{-1} + a_{1,0} Y_1^0 + a_{1,1} Y_1^1$.

of W_{lm} for all of the considered structures, where we investigate s - and p -type components $l = \{0, 1\}$ which are dominant at small and moderate q . In the case of lens-shaped [001]-oriented QD [Fig.6(a)], the main contribution comes from Y_1^1 , and considerably smaller from Y_1^{-1} . This is consistent with the results in Sec. III A, where the coupling between $M_z \approx 0$ and $M_z \approx 1$ states gives anticrossing between the energy branches. For the disk-shaped structure [Fig.6(b)], the main contribution comes from Y_1^{-1} . This clearly agrees with the spectrum considered in Sec. III B, where the selection rules allow coupling between s_2 state and nominally p state with $M_z \approx -1$, but coupling to $M_z \approx 1$ is prohibited. In the case of

[111]-oriented structure [Fig. 6(c)], the important contributions at low q come from Y_1^1 , Y_1^0 and Y_0^0 . We note, that the states are labeled as s - or p - type with respect to their dominant envelope symmetry. As discussed in Sec. III C, the selection rules forbid the coupling of s_1 , s_2 to nominally p -type states with $M_z \approx \pm 1$. However, the form-factor contains sum over envelope products from all of the subbands (which have various symmetry, including p type), and their significance depends on q . To study the importance of such contributions, we calculate spin relaxation rate due to piezoelectric coupling within two approximations. In the first one, the form-factor contains only the spherical harmonics of s -type: $F(q) \approx a_{0,0}Y_0^0$, and the second one is $F(q) \approx a_{1,-1}Y_1^{-1} + a_{1,0}Y_1^0 + a_{1,1}Y_1^1$. As shown in Fig. 7, for magnetic fields up to $B \approx 0.5$ T, the p -type contributions dominate. On the other hand, the s -type contributions have different magnetic field dependence ($\propto B^5$ vs. $\propto B^7$) and starts to dominate at higher magnetic fields. This explains the change in blue line slope visible in Fig. 5(a).

V. CONCLUSIONS

We have investigated the hole s - p coupling related to the spin-orbit interaction for three InAs/GaAs QDs representing symmetry point groups: C_{2v} , C_{3v} and D_{2d} . Using the group theory, we have identified irreducible representations of the states and explained the selection rules in the considered QDs. We have shown that in the case of [001]-oriented lens shaped QD important contribution to the width of the avoided crossing between s - and p -shell energy levels comes from the shear strain. Furthermore, we have demonstrated no coupling between nominally s - and p -type states in the [111]-oriented lens shaped QD. We calculated phonon-assisted spin relaxation rates for all of the considered structures and shown that [111]-oriented QD offers an order of magnitude longer spin lifetimes.

ACKNOWLEDGMENTS

This work was supported by the Polish National Science Centre (via Grant No. 2014/13/B/ST3/04603). Calculations have been carried out using resources provided by Wrocław Centre for Networking and Supercomputing (<http://wcss.pl>), Grant No. 203. We would like to thank Paweł Machnikowski and Michał Gawelczyk for their helpful suggestions. We are also grateful to Michał Gawelczyk for sharing his implementation of the blur algorithm.

Appendix A: Symmetry point groups

In this Appendix we present the character tables of the symmetry point groups C_{2v} , C_2 , C_{3v} , C_3 , D_{2d} and S_4 .

TABLE II. Character table of C_{2v} symmetry point group⁵³.

C_{2v}	E	\mathcal{R}	C_2+ \mathcal{RC}_2	$\sigma_v(xz)+$ $\mathcal{R}\sigma_v(xz)$	$\sigma_v(yz)+$ $\mathcal{R}\sigma_v(yz)$
A_1	1	1	1	1	1
A_2	1	1	1	-1	-1
B_1	1	1	-1	1	-1
B_2	1	1	-1	-1	1
$D_{1/2}$	2	-2	0	0	0

TABLE III. Character table of C_2 symmetry double point group⁵³.

C_2	E	C_2	\mathcal{R}	\mathcal{RC}_2
A_1	1	1	1	1
B_1	1	-1	1	-1
D_A	1	i	-1	-i
D_B	1	-i	-1	i

In the presence of spin, the double group representations are used. Here \mathcal{R} denotes the rotation of 2π , while the neutral element E corresponds to the rotation of 4π ^{46,48}. In the group C_{2v} , the two-dimensional irreducible representation $D_{1/2}$ contains diagonal matrices $\Gamma^{(D_{1/2})}(E)$, $\Gamma^{(D_{1/2})}(\mathcal{R})$, $\Gamma^{(D_{1/2})}(C_2)$, but the matrices representing reflections σ_v have off-diagonal elements. Hence, the reduction C_{2v} to subgroup C_2 leaves all $D_{1/2}$ non-diagonal matrices. In consequence it can be separated into two irreducible representations D_A , D_B .

Within the 8-band $\mathbf{k}\cdot\mathbf{p}$ model with envelope function approximation, the eigenstates of the system have a form

$$|\Psi_n\rangle = \sum_{m=1}^8 \Phi_{n,m}(\mathbf{r}) |J, J_z\rangle_m,$$

where $\Phi_{n,m}$ is the envelope and $|J, J_z\rangle_m$ describes the Bloch part (at $\mathbf{k} = 0$) with the total band angular momentum J and its axial projection J_z . The basis contains: conduction band $|\frac{1}{2}, \pm\frac{1}{2}\rangle_c$, heavy-hole $|\frac{3}{2}, \pm\frac{3}{2}\rangle_v$, light-hole $|\frac{3}{2}, \pm\frac{1}{2}\rangle_v$, and two split-off subbands $|\frac{1}{2}, \pm\frac{1}{2}\rangle_v$. To find the irreducible representation of a given state $|\Psi_n\rangle$, we performed the projection with operator $\hat{P}^{(\alpha)} = \sum_i \chi^*(\hat{R}_i) \hat{R}_i$, where $\chi(\hat{R}_i)$ is a character of the representation α for the symmetry operation \hat{R}_i ^{46,49}. As the envelope part changes slowly in scale of the unit cell, we act with \hat{R}_i on the envelope and Bloch part of the wave functions separately, e.g., the effect of axial rotation C_k is $C_k \Phi_{n,m}(\mathbf{r}) = \Phi_{n,m}(C_k^{-1}\mathbf{r})$, and $C_k |J, J_z\rangle = e^{-ij_z 2\pi/k} |J, J_z\rangle$. We express the improper rotations S_k as $S_k = \sigma_h C_k = \mathcal{I} C_2 C_k$, where σ_h is reflection in plane perpendicular to the rotation axis and \mathcal{I} is the inversion operator⁴⁸. The effect of inversion is $\mathcal{I} |\frac{1}{2}, \pm\frac{1}{2}\rangle_c = |\frac{1}{2}, \pm\frac{1}{2}\rangle_c$ for the conduction band, and $\mathcal{I} |J, J_z\rangle_v = -|J, J_z\rangle_v$ for the valence-band basis states.

TABLE IV. Character table of D_{2d} symmetry double point group⁵³.

D_{2d}	E	\mathcal{R}	$2S_4$	$2\mathcal{R}S_4$	C_2	$2C'_2$	$2\sigma_d$
A_1	1	1	1	1	1	1	1
B_1	1	1	-1	-1	1	1	-1
B_2	1	1	-1	-1	1	-1	1
E	2	2	0	0	-2	0	0
$D_{1/2}$	2	-2	$\sqrt{2}$	$-\sqrt{2}$	0	0	0
D'	2	-2	$-\sqrt{2}$	$\sqrt{2}$	0	0	0

TABLE V. Character table of S_4 symmetry double point group⁵³.

S_4	E	S_4	C_2	S_4^3	\mathcal{R}	$\mathcal{R}S_4$	$\mathcal{R}C_2$	$\mathcal{R}S_4^3$
A	1	1	1	1	1	1	1	1
B	1	-1	1	-1	1	-1	1	-1
E_1	1	i	-1	$-i$	1	i	-1	$-i$
E_2	1	$-i$	-1	i	1	$-i$	-1	i
D_I	1	$\frac{-1+i}{\sqrt{2}}$	$-i$	$\frac{1+i}{\sqrt{2}}$	-1	$\frac{1-i}{\sqrt{2}}$	i	$\frac{-1-i}{\sqrt{2}}$
D_{II}	1	$\frac{-1-i}{\sqrt{2}}$	i	$\frac{1-i}{\sqrt{2}}$	-1	$\frac{1+i}{\sqrt{2}}$	$-i$	$\frac{-1+i}{\sqrt{2}}$
D_{III}	1	$\frac{1-i}{\sqrt{2}}$	$-i$	$\frac{-1-i}{\sqrt{2}}$	-1	$\frac{-1+i}{\sqrt{2}}$	i	$\frac{1+i}{\sqrt{2}}$
D_{IV}	1	$\frac{1+i}{\sqrt{2}}$	i	$\frac{-1+i}{\sqrt{2}}$	-1	$\frac{-1-i}{\sqrt{2}}$	$-i$	$\frac{1-i}{\sqrt{2}}$

TABLE VI. Character table of C_{3v} symmetry double point group⁵³.

C_{3v}	E	\mathcal{R}	$2C_3^2$	$2\mathcal{R}C_3^2$	$3\sigma_v$	$3\mathcal{R}\sigma_v$
A_1	1	1	1	1	1	1
A_2	1	1	1	1	-1	-1
E	2	2	-1	-1	0	0
$D_{1/2}$	2	-2	1	-1	0	0
D'	1	-1	-1	1	i	$-i$
D''	1	-1	-1	1	$-i$	i

TABLE VII. Character table of C_3 symmetry double point group⁵³.

C_3	E	C_3	C_3^2	\mathcal{R}	$\mathcal{R}C_3$	$\mathcal{R}C_3^2$
A_1	1	1	1	1	1	1
B_1	1	$e^{2i\pi/3}$	$e^{4i\pi/3}$	1	$e^{2i\pi/3}$	$e^{4i\pi/3}$
B_2	1	$-e^{i\pi/3}$	$e^{2i\pi/3}$	1	$-e^{i\pi/3}$	$e^{2i\pi/3}$
D_I	1	-1	1	-1	1	-1
D_{II}	1	$e^{i\pi/3}$	$e^{i2\pi/3}$	-1	$-e^{i\pi/3}$	$-e^{i2\pi/3}$
D_{III}	1	$-e^{2i\pi/3}$	$e^{4i\pi/3}$	-1	$e^{2i\pi/3}$	$-e^{4i\pi/3}$

Appendix B: Effective model

In this part we describe the effective model that can be used to interpret the simulation results. We utilize the Fock-Darwin model supplemented by additional terms

representing system anisotropy as well as the spin-orbit coupling^{16–18}.

In the axial approximation, the states in a QD can be characterized according to their axial projection of the envelope angular momentum M_z , where the s shell contains states with $M_z = 0$ and the p shell with $M_z = \pm 1$. In fact, p -type states can be mixed due to anisotropy related to the piezoelectric potential, dot elongation and other possible effects. Due to the dominant heavy-hole components of the considered states, their axial projections of band angular momenta (\uparrow, \downarrow) can be approximated by $\langle J_z \rangle \approx \pm 3/2$. Furthermore, the spin-orbit coupling distinguishes the mutual alignment of the envelope and the band angular momenta as well as it can mix s - and the p -shell states. We express the Hamiltonian in the basis $|M_z J_z\rangle = |M_z\rangle \otimes |J_z\rangle$ and consider s and p shells $\{|0 \uparrow\rangle, |1 \uparrow\rangle, |-1 \uparrow\rangle, |0 \downarrow\rangle, |1 \downarrow\rangle, |-1 \downarrow\rangle\}$. The effective Hamiltonian reads

$$\begin{aligned}
H_{\text{eff}} = & E_s |0\rangle\langle 0| \otimes \mathbb{I}_2 + E_p (|1\rangle\langle 1| + |-1\rangle\langle -1|) \otimes \mathbb{I}_2 \\
& + V_a (|1\rangle\langle -1| + |-1\rangle\langle 1|) \otimes \mathbb{I}_2 + \frac{1}{\hbar} W B_z L_z \otimes \mathbb{I}_2 \\
& + \frac{1}{2} \mu_B [g_s |0\rangle\langle 0| + g_p (|1\rangle\langle 1| + |-1\rangle\langle -1|)] B_z \otimes \sigma_z \\
& + \frac{1}{2\hbar} V_{\text{pp}}^{(\text{so})} L_z \otimes \sigma_z \\
& + V_{\text{sp}}^{(\text{so})} (|0\rangle\langle -1| \otimes |\uparrow\rangle\langle \downarrow| + |-1\rangle\langle 0| \otimes |\downarrow\rangle\langle \uparrow|) \\
& - V_{\text{sp}}^{(\text{so})} (|0\rangle\langle 1| \otimes |\downarrow\rangle\langle \uparrow| + |1\rangle\langle 0| \otimes |\uparrow\rangle\langle \downarrow|) \\
& + \alpha_s B_z^2 |0\rangle\langle 0| \otimes \mathbb{I}_2 \\
& + \alpha_p B_z^2 (|1\rangle\langle 1| + |-1\rangle\langle -1|) \otimes \mathbb{I}_2,
\end{aligned}$$

where E_s , E_p are the bare energies ($B = 0$, axial approximation, SOC neglected) of the s - and p -type states respectively, \mathbb{I}_2 is the unit operator in the band angular momentum formal subsystem, V_a is a parameter accounting for the anisotropy, L_z is the operator of the z component of the envelope angular momentum, g_s and g_p are g -factors in s - and p -shell respectively, σ_i are the Pauli matrices, $V_{\text{pp}}^{(\text{so})}$ describes the spin-orbit coupling for the p -states, $V_{\text{sp}}^{(\text{so})}$ is a parameter related to the coupling between s and p states, finally α_s and α_p account for the diamagnetic shift. We neglect the coupling of $|0 \uparrow\rangle$ to $|1 \downarrow\rangle$, and $|0 \downarrow\rangle$ to $|-1 \uparrow\rangle$ because they are not represented by any avoided crossing in the considered spectrum. The effective Hamiltonian can be then written in matrix block form

$$H_{\text{eff}} = \begin{pmatrix} \mathcal{H}_{\text{env}} + \frac{1}{2} \mathcal{H}_1 & \mathcal{H}_2 \\ \mathcal{H}_2^\dagger & \mathcal{H}_{\text{env}} - \frac{1}{2} \mathcal{H}_1 \end{pmatrix},$$

where

$$\begin{aligned}
\mathcal{H}_{\text{env}} = & \begin{pmatrix} E_s & 0 & 0 \\ 0 & E_p + W B_z & V_a \\ 0 & V_a & E_p - W B_z \end{pmatrix} \\
& + \begin{pmatrix} \alpha_s B_z^2 & 0 & 0 \\ 0 & \alpha_p B_z^2 & 0 \\ 0 & 0 & \alpha_p B_z^2 \end{pmatrix},
\end{aligned}$$

$$\mathcal{H}_1 = \begin{pmatrix} \mu_B g_s B_z & 0 & 0 \\ 0 & \mu_B g_p B_z + V_{pp}^{(so)} & 0 \\ 0 & 0 & \mu_B g_p B_z - V_{pp}^{(so)} \end{pmatrix},$$

$$\mathcal{H}_2 = \begin{pmatrix} 0 & 0 & V_{sp}^{(so)} \\ -V_{sp}^{(so)} & 0 & 0 \\ 0 & 0 & 0 \end{pmatrix}.$$

We fitted the simulation data from Fig. 2 with the effective model and obtained the following parameters: $E_s = -229.14$ meV, $E_p = -203.75$ meV, $V_a = 0.33328$ meV, $W = -0.46764$ meV/T, $g_s = -5.5745$, $g_p = -0.11141$, $V_{pp}^{(so)} = -8.0707$ meV, $V_{sp}^{(so)} = 123.13$ μ eV, $\alpha_s = 3.0834$ μ eV/T², and $\alpha_p = 5.0050$ μ eV/T². Such parameter set gives energies in a good agreement with these obtained from the 8-band k - p model.

-
- * Krzysztof.Gawarecki@pwr.edu.pl
- ¹ I. Žutić, J. Fabian, and S. D. Sarma, Rev. Mod. Phys. **76**, 323 (2004).
 - ² R. Hanson, L. P. Kouwenhoven, J. R. Petta, S. Tarucha, and L. M. Vandersypen, Rev. Mod. Phys. **79**, 1217 (2007).
 - ³ D. Loss and D. P. DiVincenzo, Phys. Rev. A **57**, 120 (1998).
 - ⁴ E. Y. S. Joe, *Spintronics in Nanoscale Devices* (Pan Stanford Publishing, 2013).
 - ⁵ C. Flindt, A. S. Sørensen, and K. Flensberg, Phys. Rev. Lett. **97**, 240501 (2006).
 - ⁶ A. V. Khaetskii and Y. V. Nazarov, Phys. Rev. B **61**, 12639 (2000).
 - ⁷ A. V. Khaetskii and Y. V. Nazarov, Phys. Rev. B **64**, 125316 (2001).
 - ⁸ V. N. Golovach, A. Khaetskii, and D. Loss, Phys. Rev. B **77**, 045328 (2008).
 - ⁹ J. I. Climente, C. Segarra, and J. Planelles, New J. Phys. **15**, 093009 (2013).
 - ¹⁰ A. Mielnik-Pyszczoński, K. Gawarecki, M. Gawelczyk, and P. Machnikowski, Phys. Rev. B **97**, 245313 (2018).
 - ¹¹ C. Segarra, J. I. Climente, F. Rajadell, and J. Planelles, J. Phys. Condens. Matter **27**, 415301 (2015).
 - ¹² R. Winkler, *Spin-Orbit Coupling Effects in Two-Dimensional Electron and Hole Systems* (Springer, 2003).
 - ¹³ X. Zhang, Q. Liu, J.-W. Luo, A. J. Freeman, and A. Zunger, Nat. Phys. **10**, 387 (2014).
 - ¹⁴ D. V. Bulaev and D. Loss, Phys. Rev. B **71**, 205324 (2005).
 - ¹⁵ S. Avetisyan, P. Pietiläinen, and T. Chakraborty, Phys. Rev. B **85**, 153301 (2012).
 - ¹⁶ S. Avetisyan, P. Pietiläinen, and T. Chakraborty, Phys. Rev. B **88**, 205310 (2013).
 - ¹⁷ A. Manaselyan and T. Chakraborty, Eur. Lett. **88**, 17003 (2009).
 - ¹⁸ K. Gawarecki, Phys. Rev. B **97**, 235408 (2018).
 - ¹⁹ A. Mielnik-Pyszczoński, K. Gawarecki, M. Gawelczyk, and P. Machnikowski, Phys. Rev. B **97**, 1 (2018).
 - ²⁰ M. Zieliński, Y. Don, and D. Gershoni, Phys. Rev. B **91**, 085403 (2015).
 - ²¹ *Multi-Band Effective Mass Approximations*, Vol. 94 of *Lecture Notes in Computational Science and Engineering*, edited by M. Ehrhardt and T. Koprucki (Springer International Publishing, 2014).
 - ²² M. F. Doty, J. I. Climente, A. Greulich, M. Yakes, A. S. Bracker, and D. Gammon, Phys. Rev. B **81**, 035308 (2010).
 - ²³ J. M. Daniels, P. Machnikowski, and T. Kuhn, Phys. Rev. B **88**, 205307 (2013).
 - ²⁴ P.-L. Ardelt, K. Gawarecki, K. Müller, A. Waeber, A. Bechtold, K. Oberhofer, J. Daniels, F. Klotz, M. Bichler, T. Kuhn, H. Krenner, P. Machnikowski, and J. Finley, Phys. Rev. Lett. **116**, 077401 (2016).
 - ²⁵ X. Ma, G. W. Bryant, and M. F. Doty, Phys. Rev. B **93**, 245402 (2016).
 - ²⁶ R. Singh and G. Bester, Phys. Rev. Lett. **103**, 063601 (2009).
 - ²⁷ S. Schulz, S. Schumacher, and G. Czycholl, Eur. Phys. J. B **64**, 51 (2008).
 - ²⁸ E. Stock, T. Warming, I. Ostapenko, S. Rodt, A. Schliwa, J. A. Töfflinger, A. Lochmann, A. I. Toropov, S. A. Moshchenko, D. V. Dmitriev, V. A. Haisler, and D. Bimberg, Appl. Phys. Lett. **96**, 093112 (2010).
 - ²⁹ T. Mano, M. Abbarchi, T. Kuroda, B. McSkimming, A. Ohtake, K. Mitsuishi, and K. Sakoda, Appl. Phys. Express **3**, 065203 (2010).
 - ³⁰ I. A. Ostapenko, E. Stock, T. Warming, S. Rodt, A. Schliwa, M. Öztürk, J. A. Töfflinger, A. Lochmann, D. Bimberg, A. I. Toropov, S. A. Moshchenko, D. V. Dmitriev, and V. A. Haisler, J. Phys. Conf. Ser. **245**, 012003 (2010).
 - ³¹ S. Schulz, M. A. Caro, E. P. O'Reilly, and O. Marquardt, Phys. Rev. B **84**, 125312 (2011).
 - ³² O. Marquardt, E. P. O'Reilly, and S. Schulz, J. Phys. Condens. Matter **26**, 035303 (2014).
 - ³³ M. Świdorski and M. Zieliński, Phys. Rev. B **95**, 125407 (2017).
 - ³⁴ C. Lü, J. L. Cheng, and M. W. Wu, Phys. Rev. B **71**, 075308 (2005).
 - ³⁵ D. V. Bulaev and D. Loss, Phys. Rev. Lett. **95**, 076805 (2005).
 - ³⁶ L. M. Woods, T. L. Reinecke, and R. Kotlyar, Phys. Rev. B **69**, 125330 (2004).
 - ³⁷ D. Heiss, S. Schaeck, H. Huebl, M. Bichler, G. Abstreiter, J. J. Finley, D. V. Bulaev, and D. Loss, **76**, 241306(R) (2007).
 - ³⁸ M. Kroutvar, Y. Ducommun, D. Heiss, M. Bichler, D. Schuh, G. Abstreiter, and J. J. Finley, Nature **432**, 81 (2004).
 - ³⁹ P. Scarlino, E. Kawakami, P. Stano, M. Shafiei, C. Reichl, W. Wegscheider, and L. Vandersypen, Phys. Rev. Lett. **113**, 256802 (2014).
 - ⁴⁰ L. M. Roth, Phys. Rev. **118**, 1534 (1960).
 - ⁴¹ C. Segarra, J. Planelles, J. I. Climente, and F. Rajadell, New J. Phys. **17**, 033014 (2015).
 - ⁴² C. Pryor, J. Kim, L. W. Wang, A. J. Williamson, and A. Zunger, J. Appl. Phys. **83**, 2548 (1998).
 - ⁴³ G. Bester, X. Wu, D. Vanderbilt, and A. Zunger, Phys. Rev. Lett. **96**, 187602 (2006).
 - ⁴⁴ M. A. Caro, S. Schulz, and E. P. O'Reilly, Phys. Rev. B

- 91**, 075203 (2015).
- ⁴⁵ T. Eissfeller, Ph.D. thesis, Technical University of Munich, 2012.
- ⁴⁶ M. S. Dresselhaus, G. Dresselhaus, and A. A. Jorio, *Group theory : application to the physics of condensed matter* (Springer-Verlag, 2010).
- ⁴⁷ P. Yu and M. Cardona, *Fundamentals of semiconductors : physics and materials properties* (Springer, 2010).
- ⁴⁸ G. L. Bir and G. E. Pikus, *Symmetry and strain-induced effects in semiconductors* (Wiley, 1974).
- ⁴⁹ L. Piela, *Ideas of quantum chemistry* (Elsevier, 2013), Appendix C.
- ⁵⁰ K. Roszak, V. M. Axt, T. Kuhn, and P. Machnikowski, Phys. Rev. B **76**, 195324 (2007).
- ⁵¹ A. Grodecka, L. Jacak, P. Machnikowski, and K. Roszak, in *Quantum Dots Res. Dev.*, (Nova ScienceNY, 2005), p. 47.
- ⁵² J.-Y. Lee and L. Greengard, J. Comput. Phys. **206**, 1 (2005).
- ⁵³ C. J. C. J. Bradley and A. P. Cracknell, *The mathematical theory of symmetry in solids : representation theory for point groups and space groups* (Oxford, 1972).